Journal of Materials Chemistry C

ROYAL SOCIETY OF CHEMISTRY

PAPER

View Article Online
View Journal | View Issue

Cite this: J. Mater. Chem. C, 2023, 11, 10634

Non-concentration quenching and energy transfer enhanced green emission in $Ca_8SrGd(PO_4)_7:Eu^{2+},Tb^{3+}$ for near-UV white LEDs with a high color rendering index†

Shaoyu Wang,[ab] Zeyu Lyu,*[b] Zheng Lu,[ab] Lixuan Wang,[ab] Jianhui Wang,[ab] Dashuai Sun,[b] Taixing Tan,[b] Sida Shen[b] and Hongpeng You *[abc]

Received 18th May 2023,
Accepted 25th June 2023

DOI: 10.1039/d3tc01717f

rsc.li/materials-c

Compared with the well-studied energy transfer from Ce^{3+} to Tb^{3+}, the energy transfer from Eu^{2+} to Tb^{3+} has the advantage of high doping concentration of Tb^{3+}, because Eu^{2+} and Tb^{3+} tend to occupy different lattice sites. Herein, the energy transfer from Eu^{2+} to Tb^{3+} is achieved in the $Ca_8SrGd(PO_4)_7$ host for an efficient Tb^{3+} doped green phosphor. The decrease in the lifetime of Eu^{2+} emission with the increasing Tb^{3+} concentration reveals the energy transfer from the Eu^{2+} to Tb^{3+} ions. Notably, the Tb^{3+} emission of $Ca_8SrGd(PO_4)_7:Eu^{2+},Tb^{3+}$ has the strongest intensity at the unity doping ratio of Tb^{3+}, indicating a non-concentration quenching effect. The absorption efficiency in the near-ultraviolet region was increased from 6% to 75% after Eu^{2+} was doped into $Ca_8SrTb(PO_4)_7$, and the emission was enhanced by approximately six times. Consequently, a high quantum efficiency (internal: 63% and external: 51%) was achieved in $Ca_8SrTb(PO_4)_7:Eu^{2+}$. Finally, a near-ultraviolet chip excited white LED was fabricated by applying the as-prepared $Ca_8SrTb(PO_4)_7:Eu^{2+}$ as the green phosphor, with a high color rendering index of 93, and a low correlated color temperature of 3728 K. These results indicate that the presented phosphor has potential in lighting applications, providing a new perspective for developing efficient Tb^{3+} activated phosphors through energy transfer and high doping concentration.

1. Introduction

In recent years, white light emitting diodes (WLEDs) have attracted enormous attention due to low energy consumption, high efficiency, fast response and environmental friendliness.[1–5] The most common way to fabricate WLEDs is to integrate a blue LED chip with multiple phosphors (for example, green and red phosphors).[6–9] However, the fabricated WLEDs usually have a lower color rendering index (Ra) and can emit blue light that may have a harmful effect on human health. To meet the requirements of human-centric lighting, an alternative method has been proposed. This method involves combining near-ultraviolet chips with blue, green and red phosphors.[10,11] However, the design of the corresponding phosphors is more complicated than simply considering their luminescence efficiency. Attention must also be given to factors such as phosphor degradation and Stokes shift, which could potentially cause a color shift or reabsorption. Among the three phosphors, the green phosphor is of critical importance since the human eye is most sensitive to green light. Therefore, it is desirable to explore green phosphors that can be excited using near-ultraviolet light.[12–14]

Some green phosphors containing Ce^{3+} and Eu^{2+} ions, such as $La_3Br(SiS_4)_2:Ce^{3+}$ and $BaSi_7N_{10}:Eu^{2+}$, have limitations due to their structural instability and harsh synthesis conditions.[15,16] On the other hand, Tb^{3+} acts as a typical activator for green emission, resulting from its typical $^5D_4$–$^7F_5$ transition (~545 nm). With the protected 4f electrons, Tb^{3+}-doped phosphors normally possess high stability in both chemical and physical aspects.[17–21] However, their absorption efficiency is low due to the 4f–4f forbidden transition, which significantly restricts the practical application of Tb^{3+}-doped phosphors. In order to broaden the excitation spectrum of Tb^{3+}, selecting an appropriate sensitizer to facilitate energy transfer is a feasible solution. The energy transfer between Ce^{3+} and Tb^{3+} has been extensively investigated for this purpose, such as $Ca_2YZr_2(AlO_4)_3:Ce^{3+},Tb^{3+}$, $NaBaScSi_2O_7:Ce^{3+},Tb^{3+}$, $CaYAlO_4:Ce^{3+},Tb^{3+}$,

[a] School of Rare Earths, University of Science and Technology of China, Hefei 230026, P. R. China
[b] Ganjiang Innovation Academy, Chinese Academy of Sciences, Ganzhou 341000, P. R. China. E-mail: zylyu@gia.cas.cn
[c] State Key Laboratory of Rare Earth Resource Utilization, Changchun Institute of Applied Chemistry, Chinese Academy of Sciences, Changchun 130022, P. R. China. E-mail: hpyou@ciac.ac.cn

† Electronic supplementary information (ESI) available. See DOI: https://doi.org/10.1039/d3tc01717f

$SrMgY_3(SiO_4)_3F:Ce^{3+},Tb^{3+}$, and $Ca_3Lu_2Si_6O_{18}:Ce^{3+},Tb^{3+}$.[22–26] As for the emission, a practical approach to achieve high brightness is to use a suitable host that allows for higher Tb^{3+} doping without concentration quenching. However, Ce^{3+} and Tb^{3+} tend to occupy the same crystal site due to their similar valence states and ionic radii, which leads to limited Tb^{3+} doping concentration. In this regard, Eu^{2+}, which exhibits similar efficient emission to that of Ce^{3+} and tends to occupy different crystal sites, may be a more suitable sensitizer for brighter Tb^{3+}-doped phosphors. Nonetheless, there is a lack of efficient Eu^{2+}-sensitized Tb^{3+}-doped phosphors for near-ultraviolet LED applications. The ideal phosphors should meet the following requirements: (i) Eu^{2+} should be effectively excited by near-ultraviolet light and transfer the energy to Tb^{3+}, (ii) the doping concentration of Tb^{3+} should be as high as possible to achieve high brightness, and (iii) the Stokes shift should be large enough to diminish potential re-absorption of the emission from the blue phosphor.

In this study, we doped Eu^{2+} and Tb^{3+} into a phosphate matrix, $Ca_8SrGd(PO_4)_7$. According to the valence and ionic radius, Eu^{2+} occupies the sites of Sr^{2+}, while Tb^{3+} occupies the sites of Gd^{3+}. Remarkably, we achieved an efficient Tb^{3+}-doped phosphor that benefited from the energy transfer and non-concentration quenching effect. After doping Eu^{2+} into $Ca_8SrTb(PO_4)_7$, the absorption efficiency increased from 6% to 75%, resulting in emission enhancement of approximately six times. Consequently, we achieved high internal quantum efficiency (63%) and external quantum efficiency (51%) in $Ca_8SrTb(PO_4)_7:Eu^{2+}$. Finally, a near-ultraviolet chip excited white LED was fabricated by applying the as-prepared $Ca_8SrTb(PO_4)_7:Eu^{2+}$ as the green phosphor. The lighting device possessed a high color rendering index (CRI), and a low correlated colour temperature (CCT).

2. Experimental section

2.1. Materials and synthesis

A series of $Ca_8SrGd(PO_4)_7$: Eu^{2+},Tb^{3+} phosphors were synthesized by a traditional high temperature solid state reaction, using $CaCO_3$ (99.99%), $SrCO_3$ (99.99%), Gd_2O_3 (99.99%), $NH_4H_2PO_4$ (99.99%), Eu_2O_3 (99.99%), and Tb_4O_7 (99.99%) as raw materials. The raw materials were well mixed together and ground in an agate mortar for 20 minutes. The resulting mixture was then placed in an alumina crucible and heated at 900 °C for 3 hours, followed by further sintering at 1300 °C for 4 hours under a reducing atmosphere.

2.2. Materials characterization

The phase purity of the sample was analyzed using a powder X-ray diffractometer (Bruker AXS D8 Advance), under the conditions of 40 kV and 40 mA, Cu Kα (λ = 0.15405 nm), 0.02° per step, 0.07s per step from 10° to 80°. The General Structural Analysis System (GSAS) program was used for XRD Rietveld refinement. The morphologies and energy spectrum (EDS) of the samples were obtained using a JSM-IT800 high-resolution field emission scanning electron microscope (SEM). Photoluminescence spectra (PL) and excitation spectra (PLE) were recorded using a Hitachi F-7100 fluorescence spectrophotometer with a 150 W Xenon lamp. The decay curves, quantum yield (QY) and time-resolved photoluminescence (TRPL) spectra were obtained using an Edinburgh instrument FLS-1000

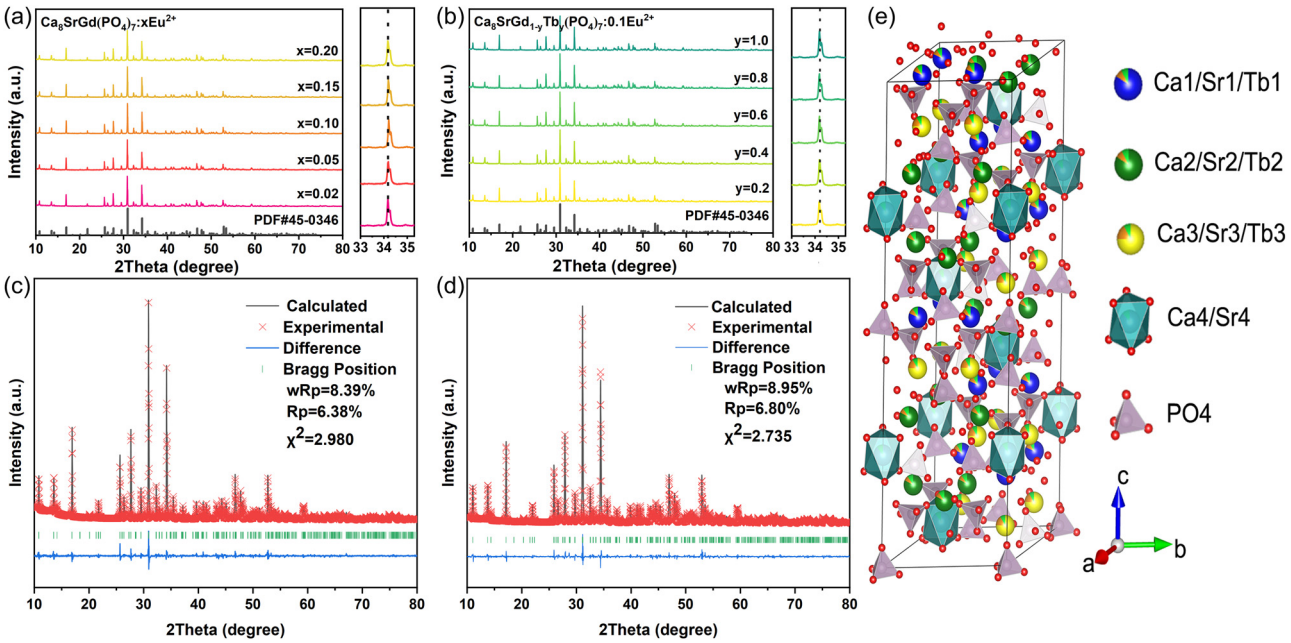

Fig. 1 XRD patterns (2θ = 10–80°) and enlarged XRD patterns at 2θ = 33–35.3° of the $Ca_8SrGd(PO_4)_7:xEu^{2+}$ (a) and $Ca_8SrGd(PO_4)_7:0.1Eu^{2+}$, yTb^{3+} (b), the Rietveld refinement results of $Ca_8SrGd(PO_4)_7$ (c) and $Ca_8SrTb(PO_4)_7:0.1Eu^{2+}$ (d), and the crystal structure of $Ca_8SrTb(PO_4)_7:0.1Eu^{2+}$ (e).

spectrometer with the Edinburgh instrument integrating sphere. The lifetimes are fitted by a second-order exponential equation. The temperature-dependent PL spectra of phosphors were obtained using an EX-1000 thermal quenching analysis system. Blue fluorescent $BaMgAl_{10}O_{17}:Eu^{2+}$, red phosphor $(Ca,Sr)AlSiN_3:Eu^{2+}$, green phosphor $Ca_8SrTb(PO_4)_7:0.1Eu^{2+}$ and a UV-LED chip (365 nm) are used to manufacture WLED devices. Starspec SSP6612 (forward bias current: 20 mA, and forward voltage: 3.36 V) was used to evaluate the luminescence characteristics of w-LED devices.

3. Results and discussion

Fig. 1a and b show the XRD patterns of $Ca_8SrGd(PO_4)_7:xEu^{2+}$ (x = 0.02, 0.05, 0.10, 0.15, and 0.20) phosphors and $Ca_8SrGd(PO_4)_7:0.1Eu^{2+}$, yTb^{3+} (y = 0.2, 0.4, 0.6, 0.8, and 1.0) phosphors, respectively. The diffraction patterns of all the as-prepared phosphors match well with the XRD pattern of $Ca_9Nd(PO_4)_7$, indicating the phase-purity of the samples. In Fig. 1(a) and (b), the XRD peaks almost remained unchanged in the 33–35.3° range, The radii of the host cations and doping ions should be almost the same, and it is reasonable to assume that Eu^{2+} replaces Sr^{2+}, and Tb^{3+} replaces Gd^{3+}. The calculated ionic radii difference percentage (Dr) is listed in Tables S1 and S2 (ESI†); the small Dr value further substantiates the substituted tendency of Eu^{2+} and Tb^{3+}. In order to further confirm the phase and crystal structure, the XRD patterns of $Ca_8SrGd(PO_4)_7$ and $Ca_8SrTb(PO_4)_7:0.1Eu^{2+}$ were refined by the Rietveld method. As shown in Fig. 1c and d, the refined results of $Ca_8SrGd(PO_4)_7$ (Rp = 6.38%, Rwp = 8.39%) and $Ca_8SrTb(PO_4)_7:0.1Eu^{2+}$ (Rp = 6.80%, Rwp = 8.95%) clarified the reliability and phase-purity. On the basis of XRD analysis, the crystal structure of the title phosphor is depicted in Fig. 1e, which has a space group of R3c and cell parameters of $a = b$ = 10.48453 Å, c = 37.554 Å, Z = 6, and V = 3575.07 Å^3 (Table S3, ESI†). These parameters are consistent with previous reports on similar hosts.[12] $Ca_8SrGd(PO_4)_7$ has four Ca sites with the coordination numbers of 8, 7, 8, and 6 for the Ca1, Ca2, Ca3, and Ca4 sites, respectively. According to the crystal structure of $Ca_9Nd(PO_4)_7$, Tb^{3+} occupies the Ca1, Ca2, and Ca3 sites. In view of similar ionic radii and charge balance of Ca^{2+} (CN = 8, r = 1.12 Å; CN = 7, r = 1.06 Å; CN = 6, r = 1.00 Å) and Sr^{2+} (CN = 8, r = 1.26 Å; CN = 7, r = 1.21 Å; CN = 6, r = 1.18 Å), it is reasonable to assume that Sr^{2+} will randomly occupy all four Ca^{2+} positions.[27] With the increasing Eu^{2+} concentration, the cell parameters of $Ca_8SrGd(PO_4)_7:xEu^{2+}$ almost remained unchanged; the variations of a, c and v were within 0.034, 0.042 and 0.099%, respectively (Fig. S1, ESI†). This observation suggests that the Eu^{2+} ions tend to replace Sr^{2+} ions due to their nearly identical ionic radii.

Fig. 2a displays scanning electron microscopy (SEM) images of the title phosphor, revealing stacked particles with sizes ranging from 2 to 6 μm. The smooth surfaces of the particles indicate their high crystallinity. The corresponding EDS spectra of $Ca_8SrTb(PO_4)_7:0.1Eu^{2+}$ phosphors are disclosed in Fig. 2b and c. According to the mass ratio, the atomic ratio was calculated to be Ca : Sr : P : Tb : Eu = 8 : 0.96 : 7.04 : 0.99 : 0.07, which matches well with the chemical formula $Ca_8SrTb(PO_4)_7:0.1Eu^{2+}$. Also, all the elements distributed uniformly in the particle.

To determine the optimal doping concentration of Eu^{2+} in $Ca_8SrGd(PO_4)_7$, the concentration dependent PL spectra were obtained. As shown in Fig. 3a, the emission profiles and position did not change, and the emission intensity reached its maximum at x = 0.10, indicating that the Eu^{2+} incorporation did not significantly alter the crystal environment. The emission of Eu^{2+} is sensitive to its surrounding crystal environment because of the exposed 5d excited orbital. Therefore, on the basis of Van Uitert's report, the Eu^{2+} occupation can be confirmed theoretically:[12,28]

$$E = Q\left[1 - \left(\frac{V}{4}\right)^{\frac{1}{v}} 10^{\frac{-nE_a r}{80}}\right] \quad (1)$$

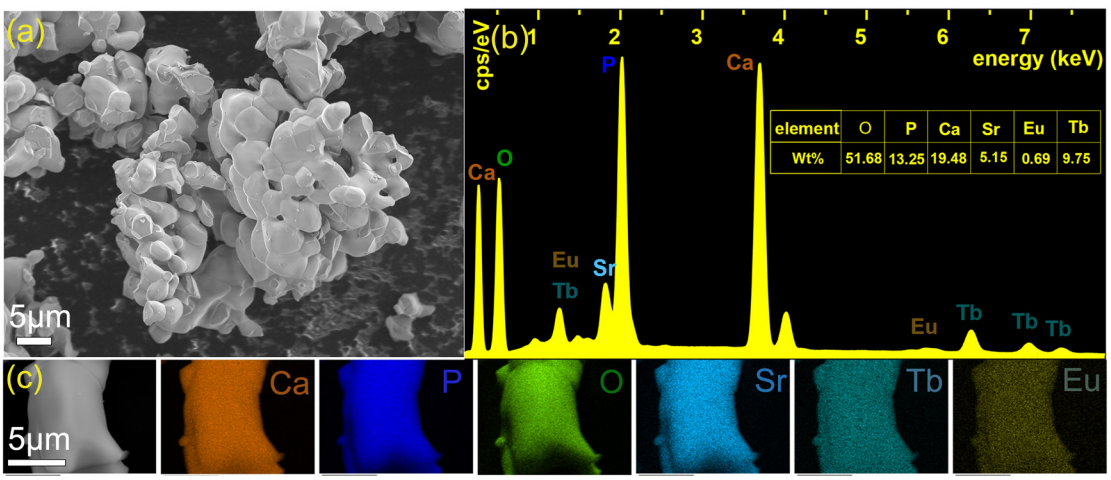

Fig. 2 SEM image of $Ca_8SrTb(PO_4)_7:0.1Eu^{2+}$ (a), EDS spectra and mass ratio of elements of $Ca_8SrTb(PO_4)_7:0.1Eu^{2+}$ (b), and elemental mappings of $Ca_8SrTb(PO_4)_7:0.1Eu^{2+}$ phosphors (c).

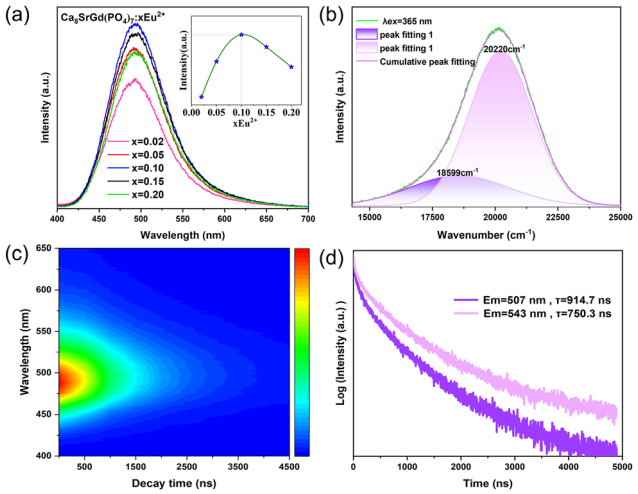

Fig. 3 (a) PL spectra of $Ca_8SrGd(PO_4)_7$: xEu^{2+}(x = 0.02, 0.05, 0.10, 0.15, and 0.20) phosphors excited at 365 nm and the inset shows the change of intensity with Eu^{2+} concentration. (b) Gaussian fitting results of the PL spectrum of $Ca_8SrGd(PO_4)_7$:$0.1Eu^{2+}$ phosphors. (c) TRPL of $Ca_8SrGd(PO_4)_7$:$0.1Eu^{2+}$. (d) Decay curves of the emissions of $Ca_8SrGd(PO_4)_7$:$0.1Eu^{2+}$ at 507 and 543 nm.

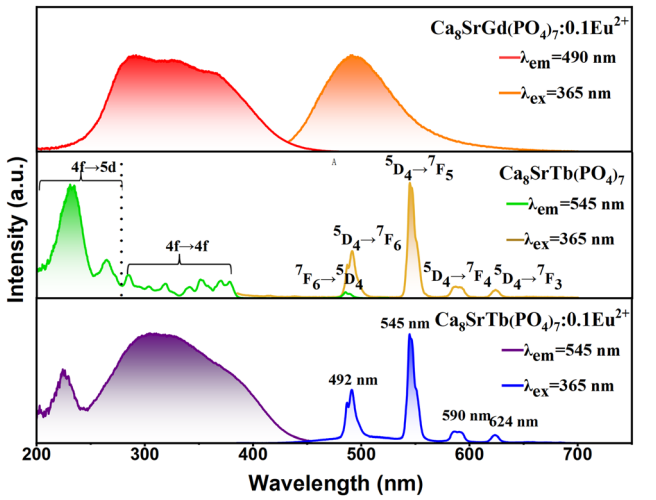

Fig. 4 PL and PLE spectra of $Ca_8SrGd(PO_4)_7$:$0.1Eu^{2+}$, $Ca_8SrTb(PO_4)_7$:$0.1Eu^{2+}$ and $Ca_8SrTb(PO_4)_7$ phosphors.

where E and Q (34 000 cm^{-1} for Eu^{2+}) represent the doped and free Eu^{2+} 5d energy level positions, respectively; V means the valence of the Eu^{2+} ion (V = 2); n is the coordination number of doped Eu^{2+}; E_a stands for the electron affinity of the atoms forming anions (E_a = 2.19 eV for the $(PO_4)^{3-}$); and r is the radius of substituted ions by Eu^{2+}. The E values of the Eu^{2+} in the Sr^{2+} sites with different coordination numbers, SrO8, SrO7, and SrO6, are determined to be 21 264 (470 nm), 19 904 (502 nm), and 18 613 cm^{-1} (537 nm), respectively (Table S4, ESI†). As shown in Fig. 3b, the asymmetric PL spectrum of $Ca_8SrGd(PO_4)_7$:$0.1Eu^{2+}$ contains two emission peaks by Gaussian fitting, which are located at 495 and 537 nm. Therefore, it is reasonable to assume that the emission peaking at 495 nm belongs to the Eu^{2+} in Sr2 (CN = 7), and the one at 537 nm belongs to Eu^{2+} in Sr4 (CN = 6). As shown in the time-resolved photoluminescence (TRPL) in Fig. 3c, the emission profiles of Eu^{2+} varied at different time intervals. The emissions at longer wavelength decayed faster than those at shorter wavelength. As a matter of fact, the emission at 507 nm possessed a lifetime of approximately 915 ns, while the one at 543 nm had a lifetime of approximately 750 ns (Fig. 3d). The inconsistent lifetimes of the emissions at different wavelengths further confirm the existence of two luminescence centers.

The occurrence of energy transfer from Eu^{2+} to Tb^{3+} requires an overlap between the Eu^{2+} emission and the Tb^{3+} excitation. The comparison among the PLE-PL spectra of $Ca_8SrGd(PO_4)_7$:$0.1Eu^{2+}$, $Ca_8SrTb(PO_4)_7$ and $Ca_8SrTb(PO_4)_7$:$0.1Eu^{2+}$ is depicted in Fig. 4. For $Ca_8SrGd(PO_4)_7$:$0.1Eu^{2+}$, its PLE spectrum monitored at 490 nm consists of a wide band from 250 to 430 nm, which matches well with that in the spectra of commercial near-ultraviolet LED chips. At 365 nm excitation, the emission covers 450–650 nm, corresponding to the transition from the $4f^65d$ excited state to the $4f^7$ ground state. For $Ca_8SrTb(PO_4)_7$, its PLE spectrum monitored at 545 nm consists of a strong band at approximately 233 nm with a shoulder at approximately 264 nm, which are attributed to the spin allowed $4f^8$–$4f^75d^1$ (ΔS = 0) and spin forbidden $4f^8$–$4f^75d^1$ (ΔS = 1) transitions, respectively.[29] In addition, there are several weak transitions from 278 to 500 nm, which can be attributed to transitions from $^7F_6$ to $^5F_{5,4}$, $^5H_{7-4}$, $^5D_{1,0}$, $^5L_{10-7}$, $^5G_{6-2}$ and $^5D_{2-4}$. Since the emission of $Ca_8SrGd(PO_4)_7$:$0.1Eu^{2+}$ overlaps with the excitation of $Ca_8SrTb(PO_4)_7$, effective energy transfer can be designed. Consequently, the PLE spectrum of $Ca_8SrTb(PO_4)_7$:$0.1Eu^{2+}$, monitored at 545 nm, shows a wide and strong excitation in the range of 200–500 nm. The PLE spectrum is composed of the excitation bands of Tb^{3+} and Eu^{2+} in the $Ca_8SrGd(PO_4)_7$ host. At excitation of 365 nm, four emission peaks at 492, 545, 594, and 624 nm in the PL spectra of $Ca_8SrTb(PO_4)_7$:$0.1Eu^{2+}$ originate from the $^5D_4$–^7F_J (J = 6, 5, 4 and 3) transitions of the Tb^{3+} ions.[29–33] The full width at half maximum (FWHM) of the emission peaking at 545 nm is only 9 nm. The smaller FWHM is capable of presenting purer colour and larger colour gamut in the display applications. Importantly, the probabilities of f–d transition are intrinsically higher than that of f–f transition. Consequently, the absorption efficiency at 350 nm increased from 6% to 75% after Eu^{2+} was doped in the $Ca_8SrTb(PO_4)_7$ (Fig. S2, ESI†). Benefiting from the energy transfer from Eu^{2+} to Tb^{3+}, the green emission of Tb^{3+} can be more effectively excited with the near-ultraviolet chip, making the Tb^{3+}-doped phosphors a potential candidate for white LEDs.

The energy transfer from Eu^{2+} to Tb^{3+} was further investigated by modulating the doping concentration. First, the doping concentration of Tb^{3+} was optimized. Strikingly, the emission of Tb^{3+} in $Ca_8SrGd(PO_4)_7$:$0.10Eu^{2+}$,yTb^{3+} kept increasing with the increasing Tb^{3+} concentration (Fig. 5a), exhibiting a non-concentration quenching effect. The fact that the optimal doping ratio of Tb^{3+} was unity substantiated the advantage of sensitizing Tb^{3+} with Eu^{2+}, due to the different doping site

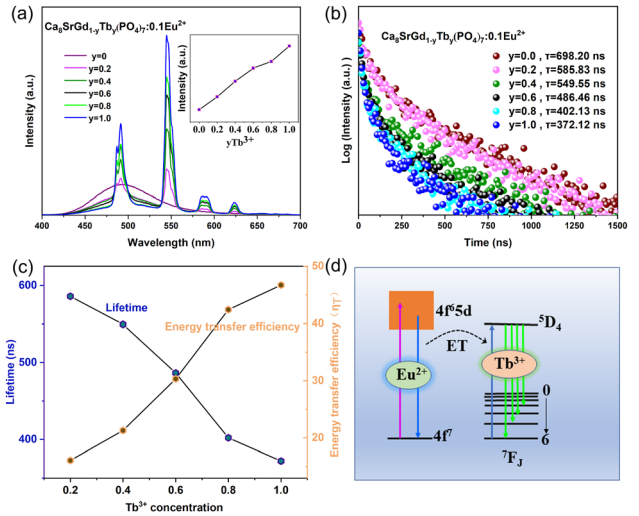

Fig. 5 (a) PL spectra of phosphor $Ca_8SrGd(PO_4)_7$:0.10Eu^{2+}, $y$$Tb^{3+}$ at 365 nm excitation and the inset shows the change of intensity with the Tb^{3+} concentration. (b) Decay curves of the emission from $Ca_8SrGd(PO_4)_7$:0.1Eu^{2+}, $y$$Tb^{3+}$ at 450 nm. (c) Changes of energy transfer efficiency and lifetime with increasing concentration of Tb ions in $Ca_8SrGd(PO_4)_7$:0.10Eu^{2+}, $y$$Tb^{3+}$. (d) Energy transfer diagram.

selectivities of these two ions. There are three main reasons for the non-concentration quenching effect of Tb^{3+} ions. One is that Tb^{3+} ions have a partially filled 4f electron shell, which is well-shielded from the surrounding environment by the 5s and 5p electron shells. This shielding reduces the interaction between Tb^{3+} ions and other ions or defects in the crystal lattice, thereby decreasing the probability of nonradiative processes that lead to concentration quenching. Another is that the larger energy gap between the ground state and excited state reduces the probability of energy transfer processes and the electron–phonon effect is significantly smaller. Lastly, and more importantly, even though there is only one Tb^{3+} ion in $Ca_8SrTb(PO_4)_7$, the Tb^{3+} ions can randomly occupy the three Ca^{2+}/Sr^{2+} sites in the crystal structure, and the Ca^{2+}/Tb^{3+} ratio is 8, resulting in a larger distance between Tb^{3+} ions. This reduces the energy transfer between Tb^{3+} ions that leads to concentration quenching. The change in the lifetime of Eu^{2+} emission upon Tb^{3+} concentration was determined to study the energy transfer efficiency.[34–38] As disclosed in Fig. 5b, the lifetime decreases monotonously with the increasing Tb^{3+} concentration. Then, the energy transfer efficiency was calculated according to the lifetime, which is the highest (46.70%) as y = 1.[39,40] Fig. 5d depicts the energy transfer diagram, where the emission of the Tb^{3+} ions is sensitized by the allowed transition between the 4f and 4f5d configuration of the Eu^{2+} ions.

The critical distance between the Eu and Tb ions can be calculated using the following formula:[41]

$$R_{Eu-Tb} = 2\left[\frac{3V}{4\Pi X_c N}\right]^{1/3} \quad (5)$$

where X_c is the critical concentration, N is the number of available bits per unit cell, and V is the volume per unit cell.

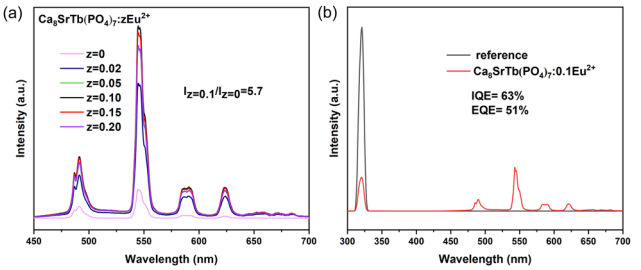

Fig. 6 (a) PL spectra of phosphor $Ca_8SrTb(PO_4)_7$:zEu^{2+} (z = 0, 0.02, 0.05, 0.10, 0.15, and 0.20) at 365 nm excitation. (b) IQE and EQE of phosphor $Ca_8SrTb(PO_4)_7$:0.1Eu^{2+} at 320 nm excitation.

For $Ca_8SrGd(PO_4)_7$, N = 6, V = 3575.07. Thus, the critical distance between Eu–Tb in $Ca_8SrGd(PO_4)_7$ is estimated to be 10.44 Å. According to the Dexter theory, we can deduce that the electric multipolar interaction dominates the energy transfer.

On the basis of the Dexter's multipole interaction energy transfer formula and Reisfeld approximation, the following relationship is established to investigate the energy transfer mechanism:[41,42]

$$\frac{\tau_{so}}{\tau} \propto C^{\frac{n}{3}} \quad (6)$$

where C is the doping amount of Tb^{3+} ions, and n = 6, 8 and 10 correspond to dipole–dipole, dipole–quadrupole and quadrupole–quadrupole interactions, respectively. The best fit occurs when n = 8, indicating that the energy of the Eu^{2+} ions transfers to the Tb^{3+} ions through dipole–quadrupole interaction (Fig. S3, ESI†).

The influence of the concentration of the Eu^{2+} ion was investigated. As disclosed in Fig. 6a, the Tb^{3+}-emission in $Ca_8SrTb(PO_4)_7$ greatly enhanced after doping with Eu^{2+}. The intensity of the Tb^{3+}-emission increases with the increasing Eu^{2+} concentration until z = 0.1, and then decreases. The change tendency is consistent with the concentration-dependent PL spectra of $Ca_8SrGd(PO_4)_7$:xEu^{2+} shown in Fig. 6a. Notably, the emission intensity of $Ca_8SrTb(PO_4)_7$:0.1Eu^{2+} was 5.7 times stronger than that of $Ca_8SrTb(PO_4)_7$. Moreover, the quantum efficiency of $Ca_8SrTb(PO_4)_7$:0.1Eu^{2+} was determined, where the internal quantum efficiency (IQE) and external quantum efficiency (EQE) at 320 nm excitation are 63% and 51%, respectively (Fig. 6b). The quantum efficiencies of some green phosphors were compared and are summarized in Table S5 (ESI†). The quantum efficiency of $Ca_8SrTb(PO_4)_7$:0.1 Eu^{2+} was comparable with that of the reported

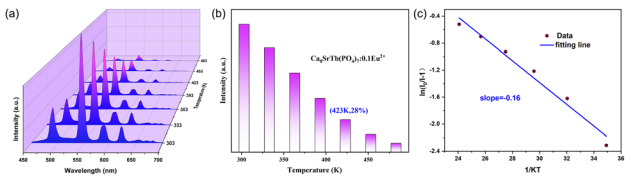

Fig. 7 (a) Temperature-dependent PL spectra (λ_{ex} = 365 nm) of $Ca_8SrTb(PO_4)_7$:0.1Eu^{2+} in the 303–483 K temperature range. (b) Emission intensity of $Ca_8SrTb(PO_4)_7$:0.1Eu^{2+} with increasing temperature. (c) Relationship between $\ln(I_0/I - 1)$ and $1/kT$ of $Ca_8SrTb(PO_4)_7$:0.1Eu^{2+}.

green phosphors, and the fine QY indicates its potential application as a green phosphor in WLEDs.[43–45]

Fig. 7a shows the temperature-dependent PL spectra in the range of 303 to 483 K. The emission profile has not changed, while the emission intensity decreases with the increase of temperature (Fig. 7b). The emission intensity at 423 K is 28% of that at 303 K. The activation energy (ΔE) of $Ca_8SrTb(PO_4)_7$:$0.1Eu^{2+}$ for thermal quenching can be determined using the following expression:[46,47]

$$\frac{I}{I_0} = \left[1 + C\exp\left(-\frac{\Delta E}{KT}\right)\right]^{-1} \quad (7)$$

where I_0 and I are emission intensities at 303 K and applied temperature, respectively; C is a constant; and k is the Boltzmann constant. ΔE could be obtained from the relationship between $\ln(I_0/I - 1)$ and $1/kT$, and the value of ΔE was the slope of the fitting line of data points (see Fig. 7c). The slope of the fitting line was found to be −0.16, indicating that the value of ΔE for $Ca_8SrGd(PO_4)_7$:$0.1Eu^{2+}$, $1.0Tb^{3+}$ phosphors was 0.16. Poorer thermal stability may come from poorer crystallinity and lower structural rigidity. The poorer crystallinity means that the arrangement of atoms or ions in the crystal lattice is not well-defined, leading to defects and disordered regions. These defects can act as quenching centers that facilitate nonradiative processes and result in the loss of luminescence. In general, the high structural rigidity of the host material will inhibit soft phonon patterns that lead to non-radiative relaxation of the activator. In $Ca_8SrGd(PO_4)_7$, there are more ions in the high coordination environment, and the larger the ionic radius, the weaker the binding force between different ions. This results in lower structural rigidity. The improvement of crystallinity and structural rigidity is often the key factor to improve thermal stability, which can be started by optimizing the synthesis process.

Finally, a white LED was fabricated with the commercial blue phosphor ($BaMgAl_{10}O_{17}$:Eu^{2+}), red phosphor ((Ca,Sr)$AlSiN_3$:Eu^{2+}) and the as-prepared green phosphor ($Ca_8SrTb(PO_4)_7$:$0.1Eu^{2+}$). Fig. 8a shows the emission spectrum under 220 mA current drive, exhibiting the characteristic green emission of the Tb^{3+} ions. The CCT of the white LED device is 3728 K, and the CRI is 93, which shows the potential for application in white LED lighting. The CIE coordinates are (0.3860, 0.3621) (Fig. 8b). In addition, the emission driven by different currents (20 mA–300 mA) was also measured, as shown in Fig. 8c, which exhibited a small shift of color. Also, the changes in CCT, CRI, efficiency, and output power under different current drives were measured (Fig. 8d and Table S6, ESI†). In the range of 20 mA–300 mA, all the CRI were greater than 85, and all the CCT were lower than 4000 K, indicating the fine quality of the as-fabricated WLED.

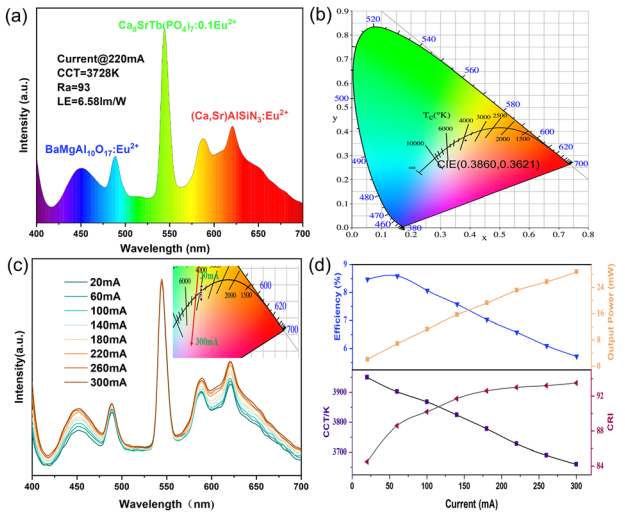

Fig. 8 (a) Emission spectrum of a white LED driven by 220 mA. (b) CIE chromaticity diagram of the fabricated white LED device driven by 220 mA. (c) Emission spectra driven by different currents and the illustration shows the change of color coordinates driven by a current in the range of 20–300 mA. (d) Change of CCT, CRI, efficiency and output power under different driving currents.

Conclusions

In summary, a novel green phosphor $Ca_8SrTb(PO_4)_7$:Eu^{2+} for white LED was successfully prepared by a traditional high temperature solid phase method. The crystal structure and morphology were analyzed by XRD and SEM, respectively. On the basis of the overlap between the PL spectrum of $Ca_8SrGd(PO_4)_7$:Eu^{2+} and the PL spectrum of $Ca_8SrTb(PO_4)_7$, the energy transfer from Eu^{2+} to Tb^{3+} was achieved with the highest energy transfer efficiency of 46.7%. Through the achieved energy transfer, a wide and strong excitation band of the Tb^{3+} emission in the range of 200–430 nm was obtained, which matched well with that of the near-ultraviolet LED chip. Moreover the absorption efficiency in the near-ultraviolet region increased from 6% to 75% after doping Eu^{2+} ions into $Ca_8SrTb(PO_4)_7$. The Tb^{3+} emission did not exhibit concentration quenching in $Ca_8SrGd(PO_4)_7$:Eu^{2+}, leading to a green phosphor with high quantum efficiencies (IQE = 63% and EQE = 51%). Finally, We used the as-prepared phosphor, $BaMgAl_{10}O_{17}$:Eu^{2+}, (Ca,Sr)$AlSiN_3$:Eu^{2+}, and a near-UV chip (365nm) to produce a white LED with a low CCT of 3728 K and a high CRI of 93. Our work not only produced a green phosphor with fine luminescent properties, but also provided an approach for developing Tb^{3+} activated phosphors with high brightness through energy transfer and non-concentration quenching.

Author contributions

Shaoyu Wang: data curation, investigation, and writing – original draft preparation. Zeyu Lyu: data curation and writing – review & editing. Zheng Lu: investigation. Lixuan Wang: data curation. Jianhui Wang: data curation. Dashuai Sun: investigation. Taixing Tan: investigation. Sida Shen: investigation. Hongpeng You: project administration, writing – review & editing, and funding acquisition.

Conflicts of interest

The authors declare no conflicts of interest.

Acknowledgements

This work is financially supported by the National Key Research and Development Program (Grant No. 2022YFC2905201), the National Natural Science Foundation of China (Grant No. 52072363), and the Research Projects of Ganjiang Innovation Academy, Chinese Academy of Sciences (E255C001).

References

1 X. Huang, J. Liang, S. Rtimi, B. Devakumar and Z. Zhang, *Chem. Eng. J.*, 2021, **405**, 126950.
2 L. Wu, S. Sun, Y. Bai, Z. Xia, L. Wu, H. Chen, L. Zheng, H. Yi, T. Sun, Y. Kong, Y. Zhang and J. Xu, *Adv. Opt. Mater.*, 2021, **9**, 2100870.
3 P. Dang, G. Li, X. Yun, Q. Zhang, D. Liu, H. Lian, M. Shang and J. Lin, *Light: Sci. Appl.*, 2021, **10**, 29.
4 A. J. van Bunningen, A. D. Sontakke, R. van der Vliet, V. G. Spit and A. Meijerink, *Adv. Opt. Mater.*, 2023, **11**, 2202794.
5 H. Daicho, T. Iwasaki, K. Enomoto, Y. Sasaki, Y. Maeno, Y. Shinomiya, S. Aoyagi, E. Nishibori, M. Sakata, H. Sawa, S. Matsuishi and H. Hosono, *Nat. Commun.*, 2012, **3**, 1132.
6 M. Shang, S. Liang, N. Qu, H. Lian and J. Lin, *Chem. Mater.*, 2017, **29**, 1813–1829.
7 W. R. Liu, C. H. Huang, C. W. Yeh, J. C. Tsai, Y. C. Chiu, Y. T. Yeh and R. S. Liu, *Inorg. Chem.*, 2012, **51**, 9636–9641.
8 J. Qiao, Z. Zhang, J. Zhao and Z. Xia, *Inorg. Chem.*, 2019, **58**, 5006–5012.
9 P. Pust, V. Weiler, C. Hecht, A. Tucks, A. S. Wochnik, A. K. Henss, D. Wiechert, C. Scheu, P. J. Schmidt and W. Schnick, *Nat. Mater.*, 2014, **13**, 891–896.
10 R. Gautier, X. Li, Z. Xia and F. Massuyeau, *J. Am. Chem. Soc.*, 2017, **139**, 1436–1439.
11 C. Wang, Z. Wang, P. Li, J. Cheng, Z. Li, M. Tian, Y. Sun and Z. Yang, *J. Mater. Chem. C*, 2017, **5**, 10839–10846.
12 R. Mi, Y. Liu, L. Mei, X. Min, M. Fang, X. Wu, Z. Huang and C. Chen, *Chem. Eng. J.*, 2023, **457**, 141377.
13 S. Hariyani, X. Xing, M. Amachraa, J. Bao, S. P. Ong and J. Brgoch, *Adv. Opt. Mater.*, 2023, **11**, 2202689.
14 S. Kumar, J. Jagielski, N. Kallikounis, Y. H. Kim, C. Wolf, F. Jenny, T. Tian, C. J. Hofer, Y. C. Chiu, W. J. Stark, T. W. Lee and C. J. Shih, *Nano Lett.*, 2017, **17**, 5277–5284.
15 S. P. Lee, S. D. Liu, T. S. Chan and T. M. Chen, *ACS Appl. Mater. Interfaces*, 2016, **8**, 9218–9223.
16 J. Qin, H. Zhang, B. Lei, H. Dong, Y. Liu, J. Meng, M. Zheng and Y. Xiao, *J. Lumin.*, 2014, **152**, 230–233.
17 Y. Li, Y. Zhou, X. Li, H. Wu, L. Zhao and W. Wang, *Spectrochim. Acta, Part A*, 2021, **252**, 119548.
18 S. Zhang, B. Qiu, Z. Li, Y. Lv, X. Chen, H. Lian, Y. Hu and Y. Li, *Chem. Eng. J.*, 2021, **426**, 130734.
19 J. J. Joos, D. Van der Heggen, L. Martin, L. Amidani, P. F. Smet, Z. Barandiaran and L. Seijo, *Nat. Commun.*, 2020, **11**, 3647.
20 L. Sun, B. Devakumar, J. Liang, S. Wang, Q. Sun and X. Huang, *J. Mater. Chem. C*, 2019, **7**, 10471–10480.
21 R. C. Knighton, L. K. Soro, L. Frances-Soriano, A. Rodriguez-Rodriguez, G. Pilet, M. Lenertz, C. Platas-Iglesias, N. Hildebrandt and L. J. Charbonniere, *Angew. Chem., Int. Ed.*, 2022, **61**, e202113114.
22 G. Li, Y. Wang, W. Zeng, W. Chen, S. Han, H. Guo and Y. Li, *J. Mater. Chem. C*, 2016, **4**, 3304–3312.
23 L. Zhou, J. Hong, X. Li, J. Shi, P. A. Tanner, K. L. Wong and M. Wu, *Adv. Opt. Mater.*, 2020, **8**, 2000523.
24 Q. Ni, J. Huo, J. Liu, H. Yan, Q. Zhu, J. Li, C. Long and Q. Wang, *Inorg. Chem. Front.*, 2022, **9**, 6584–6595.
25 Z. Lu, D. Sun, Z. Lyu, S. Shen, L. Wang, J. Wang, H. Zhao and H. You, *J. Am. Ceram. Soc.*, 2022, **106**, 1182–1193.
26 Y. Xiao, Z. Hao, L. Zhang, X. Zhang, G.-H. Pan, H. Wu, H. Wu, Y. Luo and J. Zhang, *J. Mater. Chem. C*, 2018, **6**, 5984–5991.
27 P. Dang, G. Li, S. Liang, H. Lian and J. Lin, *J. Mater. Chem. C*, 2019, **7**, 5975–5987.
28 X. Ding, G. Zhu, W. Geng, M. Mikami and Y. Wang, *J. Mater. Chem. C*, 2015, **3**, 6676–6685.
29 L. Jiang, R. Pang, D. Li, W. Sun, Y. Jia, H. Li, J. Fu, C. Li and S. Zhang, *Dalton Trans.*, 2015, **44**, 17241–17250.
30 D. Zhao, Y. Xue, R. Zhang, B. Liu, Y. Fan, S. Dai, S. Zhang and Z. Ma, *Inorg. Chem. Front.*, 2020, **7**, 667–677.
31 X. Wu, R. Shi, J. Zhang, D. Wen, Z. Qiu, X. Zhang, W. Zhou, L. Yu and S. Lian, *Chem. Eng. J.*, 2022, **429**, 132225.
32 F. Meng, Z. Dehouche, T. G. Ireland and G. R. Fern, *Prog. Photovoltaics*, 2019, **27**, 640–651.
33 W. Zhao, S. Gao, S. An, B. Fan and S. Li, *Chin. Sci. Bull.*, 2012, **57**, 4513–4516.
34 N. Wang, T. Li, L. Han, Y. Wang, Z. Ci, Y. Wang and H. Jiao, *J. Mater. Sci.*, 2019, **54**, 6434–6450.
35 C. Zhong, Y. Xu, X. Wu, S. Yin, X. Zhang, L. Zhou and H. You, *J. Mater. Chem. C*, 2023, **11**, 3375–3385.
36 J. Yang, P. He, Y. Xie, Q. Chen, Q. Dong, W. Nie, F. Yang, W. Wang, F. Du, J. Peng and X. Ye, *J. Alloys Compd.*, 2022, **903**, 163815.
37 S. Miao, Y. Liang, D. Chen, S. Yan, J. Liu, W. Wang and J. Bi, *J. Mater. Chem. C*, 2022, **10**, 14211–14219.
38 S. Wu, P. Xiong, Q. Liu, Y. Xiao, Y. Sun, E. Song and Y. Chen, *Adv. Opt. Mater.*, 2022, **10**, 2201718.
39 Y. Zhang, S. Miao, Y. Liang, C. Liang, D. Chen, X. Shan, K. Sun and X. J. Wang, *Light: Sci. Appl.*, 2022, **11**, 136.
40 I. Carrasco, F. Piccinelli and M. Bettinelli, *J. Phys. Chem. C*, 2017, **121**, 16943–16950.

41 T. Zhang, X. Jiang, R. Chen, B. Liu, W. Yang, C. Li, H. Lin, H. Liu, C. Li, F. Zeng and Z. Su, *Inorg. Chem. Front.*, 2022, **9**, 6418–6424.
42 J. Zhang, X. Zhang, J. Zhang, W. Ma, X. Ji, S. Liao, Z. Qiu, W. Zhou, L. Yu and S. Lian, *J. Mater. Chem. C*, 2017, **5**, 12069–12076.
43 R. Cao, D. Peng, H. Xu, S. Jiang, Z. Luo, H. Ao and P. Liu, *J. Lumin.*, 2016, **178**, 388–391.
44 J. Zhong, D. Chen, Y. Yuan, L. Chen, H. Yu and Z. Ji, *Chem. Eng. J.*, 2017, **309**, 795–801.
45 J. Li, X. Zhou, J. Ding, X. Zhou and Y. Wang, *J. Mater. Chem. C*, 2019, **7**, 2257–2266.
46 Z. Liao, H. Xu, W. Zhao, H. Yang, J. Zhong, H. Zhang, Z. Nie and Z.-K. Zhou, *Chem. Eng. J.*, 2020, **395**, 125060.
47 X. Qin, X. Liu, W. Huang, M. Bettinelli and X. Liu, *Chem. Rev.*, 2017, **117**, 4488–4527.